

Superstructures generated from truncated tetrahedral quantum dots

Yasutaka Nagaoka¹, Rui Tan¹, Ruipeng Li^{2,6}, Hua Zhu¹, Dennis Eggert^{3,4}, Yimin A. Wu⁵, Yuzi Liu⁵, Zhongwu Wang² & Ou Chen^{1*}

The assembly of uniform nanocrystal building blocks into well ordered superstructures is a fundamental strategy for the generation of meso- and macroscale metamaterials with emergent nanoscopic functionalities^{1–10}. The packing of spherical nanocrystals, which frequently adopt dense, face-centred-cubic or hexagonal-close-packed arrangements at thermodynamic equilibrium, has been much more widely studied than that of non-spherical, polyhedral nanocrystals, despite the fact that the latter have intriguing anisotropic properties resulting from the shapes of the building blocks^{11–13}. Here we report the packing of truncated tetrahedral quantum dot nanocrystals into three distinct superstructures—one-dimensional chiral tetrahelices, two-dimensional quasicrystal-approximant superlattices and three-dimensional cluster-based body-centred-cubic single supercrystals—by controlling the assembly conditions. Using techniques in real and reciprocal spaces, we successfully characterized the superstructures from their nanocrystal translational orderings down to the atomic-orientation alignments of individual quantum dots. Our packing models showed that formation of the nanocrystal superstructures is dominated by the selective facet-to-facet contact induced by the anisotropic patchiness of the tetrahedra. This study provides information about the packing of non-spherical nanocrystals into complex superstructures, and may enhance the potential of self-assembled nanocrystal metamaterials in practical applications.

Packing shapes are of interest for various disciplines, ranging from pure mathematics to industrial design, and have long been a subject of active research^{14–19}. Even the simplest Platonic shape, the tetrahedron, becomes complicated when packed in a defined space because it does not tile in the three-dimensional (3D) space of Euclidean geometry^{16,17}. After it was proposed that tetrahedra might possess the lowest packing density of any convex shape¹⁸, their arrangement into dense phases became of interest^{11,16–19}. So far, considerable progress has been made in the mathematical constructions of tetrahedral packing^{11,16–19}; this includes the seminal work on packing tetrahedra in a quasicrystalline fashion (82-tetrahedron unit cell) through exclusive, shape-induced, entropic interactions¹¹.

Unlike the extensive mathematical studies, there have been very few reports of experimental achievements in this area^{20–24}. Complex superstructures of packed tetrahedra, such as that predicted in ref. ¹¹, have not yet been observed experimentally. Here we report that three distinct superstructures—from 1D to 3D—can be obtained by self-assembly of truncated tetrahedral quantum dots (TTQDs). Although the 2D superlattices can be only tentatively assigned on the basis of the current data, our observation expands the collection of superstructures that can be constructed from tetrahedral building blocks. More importantly, our findings bring the spontaneous formation of nanocrystal assemblies to a higher level of complexity.

Monodispersed wurtzite (WZ) TTQDs were synthesized according to a previously published method with modifications²⁵. Transmission electron microscopy (TEM) revealed that the TTQDs are tetrahedral in shape with slightly truncated edges (Fig. 1a–c, Extended Data

Fig. 1). The average inorganic height of the tetrahedra is 6.7 ± 0.4 nm along the $[0002]_{\text{WZ}}$ direction (Supplementary Figs. 1, 2). The bottom $\{0002\}_{\text{WZ}}$ facet (red in the model shown in Fig. 1) is coated with octadecylphosphonic acid (ODPA), and three equivalent side $\{10\bar{1}1\}_{\text{WZ}}$ facets (blue in the model) are coated with oleic acid²⁵ (Fig. 1d, Supplementary Figs. 3–6, Supplementary Tables 1, 2). Including the surface organic ligands, the effective shape of the building blocks can be considered as a tetrahedron with an edge length l of 10.3 ± 0.4 nm (Fig. 1d).

The superstructures can be formed by drop-casting a solution of TTQDs in hexane onto a TEM grid placed on a silicon wafer (see Methods). When using relatively low particle concentrations (around 0.2 mg ml⁻¹), the predominant species formed are 1D linear TTQD assemblies (Fig. 1e) with a tetrahelical (also called a ‘Bernal spiral’) structure. The typical width of the helix ranges from 6.3 to 6.7 nm, with lengths of up to 150 nm (approximately 46 TTQDs) (Supplementary Figs. 7–12, Supplementary Tables 3–5). Figure 1f shows an example of one right-handed tetrahelix with seven interconnected TTQDs showing five consecutive atomic domains. The fast Fourier transformation (FFT) of the five atomic domains well matches the simulated FFT pattern that was based on our proposed tetrahelical model (Fig. 1f, g, Supplementary Table 3). In the model, the TTQDs are connected through defined facet-to-facet contact in a clockwise spiral (that is, $\{0002\}_{\text{WZ}}$ -to- $\{0002\}_{\text{WZ}}$ or $\{10\bar{1}1\}_{\text{WZ}}$ -to- $\{10\bar{1}1\}_{\text{WZ}}$). In addition, left-handed tetrahelices (with a counter-clockwise spiral) were also observed (Extended Data Fig. 2, Supplementary Table 5).

Controlled evaporation of a TTQD/hexane solution with a high particle concentration (around 20 mg ml⁻¹) in a glass vial led to the formation of sub-millimetre, 3D single supercrystals (Supplementary Figs. 13–15). Synchrotron-based small-angle and wide-angle X-ray scattering (SAXS and WAXS, respectively) experiments were conducted to fully elucidate the structure, with a coherence of translational alignment and orientational ordering¹³. Initially, one piece of the TTQD supercrystal was aligned in the $[001]_{\text{bcc}}$ orientation (bcc, body-centred cubic) and rotated along the $[110]_{\text{bcc}}$ axis, with a step angle of 1° (Fig. 2a). A comprehensive set of SAXS and WAXS images was collected simultaneously from the single supercrystal (Supplementary Videos 1 and 2). The SAXS data reveal a single-crystalline dotted pattern indicative of a bcc crystal phase (Supplementary Video 1). Figure 2b–m shows the SAXS and WAXS 2D images at three representative crystallographic orientations—that is, $[001]_{\text{bcc}}$, $[\bar{1}11]_{\text{bcc}}$ and $[\bar{1}10]_{\text{bcc}}$ —for rotation angles θ of 0° , 55° and 90° along the $[110]_{\text{bcc}}$ axis. The orders of rotational symmetry are the same on both the atomic scale (WAXS) and the mesoscale (SAXS); that is, four-, six- and two-fold symmetries at $[001]_{\text{bcc}}$, $[\bar{1}11]_{\text{bcc}}$ and $[\bar{1}10]_{\text{bcc}}$ projections, respectively. Notably, the calculated unit-cell lattice parameter of the obtained bcc supercrystals is 38.1 ± 0.3 nm (Extended Data Fig. 3, Supplementary Tables 6–8), which is about four times as large as the effective edge length of the TTQD building block (10.3 ± 0.4 nm). This large discrepancy suggests that the unit cell of the bcc supercrystal is

¹Department of Chemistry, Brown University, Providence, RI, USA. ²Cornell High Energy Synchrotron Source, Cornell University, Ithaca, NY, USA. ³Max Planck Institute for the Structure and Dynamics of Matter, Hamburg, Germany. ⁴Heinrich Pette Institute, Leibniz Institute for Experimental Virology, Hamburg, Germany. ⁵Center for Nanoscale Materials, Argonne National Laboratory, Argonne, IL, USA. ⁶Present address: National Synchrotron Light Source II, Brookhaven National Laboratory, Upton, NY, USA. *e-mail: ouchen@brown.edu

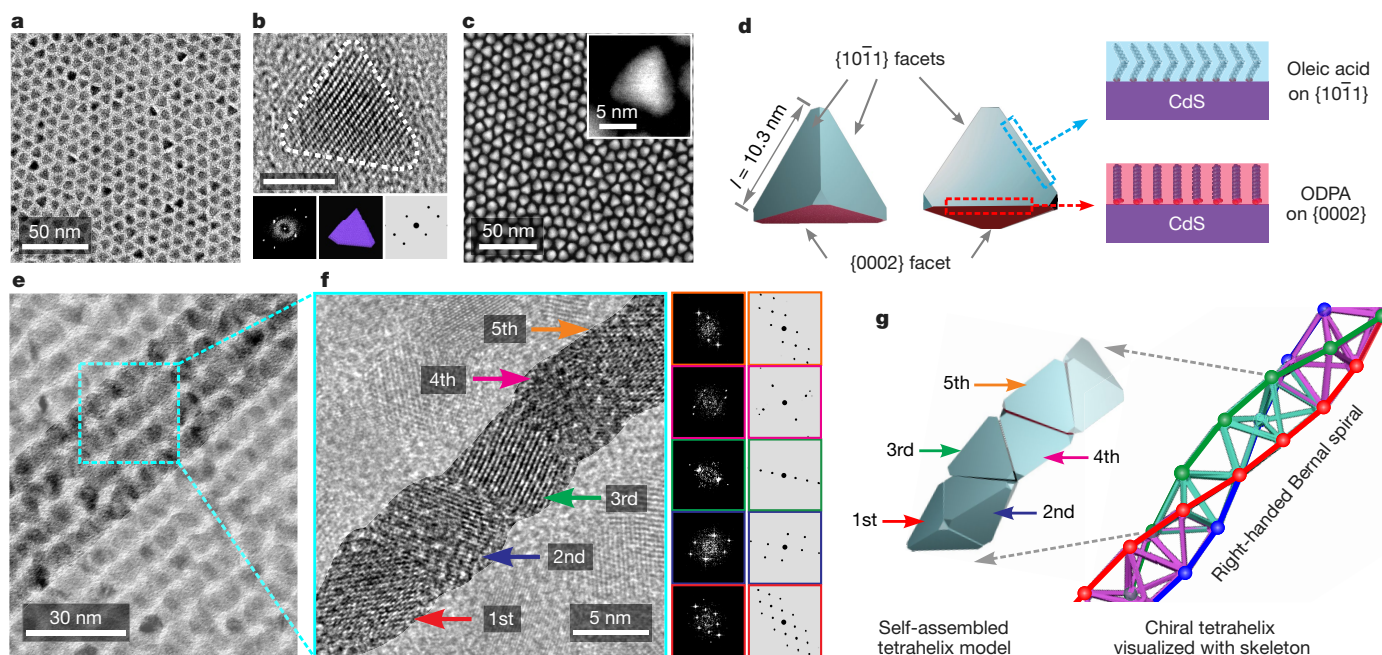


Fig. 1 | Characterization of the TTQD building blocks and tetrahedral assemblies. **a**, TEM image of TTQDs. **b**, High-resolution (HR)-TEM image (top) of an individual TTQD, the corresponding FFT pattern (bottom left) and the atomic model (bottom centre) with its corresponding simulated electron diffraction pattern (bottom right). Scale bar, 4 nm. **c**, High-angle annular dark-field imaging (HAADF)-TEM images of TTQDs. **d**, Schematic of an effective tetrahedral shape of TTQDs with an edge length of 10.3 ± 0.4 nm. The tetrahedron exhibits three $\{10\bar{1}1\}$ facets and one $\{0002\}$ facet. Oleic acid and ODPa were bound mainly on the

$\{10\bar{1}1\}$ facets (blue) and the $\{0002\}$ facet (red), respectively. **e**, TEM image of tetrahedral assemblies. **f**, HR-TEM image of a tetrahedral assembly (left), the FFT patterns corresponding to the five consecutive domains (middle) and their corresponding simulated electron diffraction patterns (right). **g**, Corresponding model of the tetrahedral assembly (left) and a skeleton visualization showing only the right-handed Bernal spiral of the chiral tetrahelix (right). We note that, owing to the overlapping of domains, only five atomic domains can be observed from seven interconnected TTQDs, as shown in **g**.

not directly formed from individual TTQDs, which was further evidenced by the computer-simulated SAXS patterns²⁶.

Recently, clathrate colloidal architectures have been assembled from DNA-modified triangular bipyramids through preformed, lower-symmetry configuration clusters⁴. In light of this finding we propose that, during the formation of the bcc supercrystals, the TTQDs first form clusters due to facet-to-facet contact ($\{0002\}_{WZ}$ -to- $\{0002\}_{WZ}$ or $\{10\bar{1}1\}_{WZ}$ -to- $\{10\bar{1}1\}_{WZ}$), and then pack into the observed bcc supercrystals at thermodynamic equilibrium^{13–15}.

On the basis of this idea, six different TTQD crystal domains were identified using a cluster model of 36 TTQDs with centering positions of $(3^2 4^5 1^2 6^2)$ (Fig. 2n, Extended Data Fig. 4, Supplementary Fig. 16). Each of the facet-contacted TTQD pairs with the same orientation is shown by a different colour and represents one particular crystal domain (Fig. 2n). Together, they assemble into the cluster unit with the long axis (indicated by the grey dashed-arrow in Fig. 2o) parallel with the $\{0002\}_{WZ}$ orientation of the grey TTQD pair (Fig. 2n). In addition, the rotational SAXS and WAXS measurements reveal that the long axis of the cluster is aligned in the $[110]_{bcc}$ direction, indicating a 45° offset from the $[001]_{bcc}$ Cartesian axis (Fig. 2o). Knowing the relative geometrical relationship, the unit cell of the bcc supercrystal can be constructed to be consistent with the abnormally large lattice parameter (38.1 ± 0.3 nm) calculated from the SAXS data (Fig. 2o). This proposed cluster-based bcc-supercrystal model can replicate the SAXS patterns (Supplementary Figs. 17–20) and well reproduce the WAXS signals with the corresponding rotational symmetries (along the $[110]_{bcc}$ and $[001]_{bcc}$ axes) in all projections (Fig. 2e, i, m, Extended Data Fig. 5, Supplementary Fig. 21). All other cluster models observed in the clathrate crystals, as well as simple icosahedron packing, were also examined and were ruled out on the basis of the size and crystal orientations of the cluster.

To better understand the superstructure, we fabricated a monolayer of cluster units of bcc supercrystals (Fig. 2p, Supplementary Fig. 22). The corresponding small- and wide-angle electron diffraction (SAED

and WAED) patterns are nearly identical to those of the SAXS and WAXS signals collected from the $[110]_{bcc}$ orientation (Fig. 2p, Extended Data Fig. 6), which suggests that the observed superlattice pattern is viewed along the $[110]_{bcc}$ direction. The lattice fringes exhibit a tri-line (strong–weak–weak) periodicity (Fig. 2p, Supplementary Fig. 22). The lattice distance between two adjacent strong lines, which are evenly divided by two weak lines, is 27.1 nm (Fig. 2p). This unusual tri-line-type lattice fringe is also observed at the edge of the bcc supercrystals (Extended Data Fig. 7) and can be explained by our cluster model with three-layer stacking at this projection (Supplementary Fig. 23). In addition, sequential rotations along the horizontal and vertical axes—by 34.3° and 45.0° , respectively—reveal the $[\bar{1}11]_{bcc}$ and $[100]_{bcc}$ orientations from the TEM images and the corresponding FFT patterns (Extended Data Fig. 8, Supplementary Fig. 24), which are consistent with the geometric relationships in a bcc crystal structure. Together, these real-space TEM observations directly verify the cluster-based bcc supercrystal model that was proposed on the basis of reciprocal space measurements from SAXS and WAXS.

We next explored other packing possibilities. When a TTQD solution with a concentration of around 2 mg ml^{-1} was evaporated, a 2D superlattice thin-film was formed with superlattice fringes of 9.4 nm (Fig. 3a, Supplementary Fig. 25). The corresponding SAED measurement reveals six-fold symmetry with a selection rule of $\{h\bar{h}00\}$ ²⁷ (Fig. 3a, Supplementary Fig. 25). Notably, the WAED exhibits a pattern with quasi-four-fold symmetry from the $(10\bar{1}0)_{WZ}$, $(10\bar{1}1)_{WZ}$ and $(11\bar{2}0)_{WZ}$ diffractions, and the $(0002)_{WZ}$ signal is absent (Fig. 3b). This symmetry discrepancy between the atomic orientation and the superstructure indicates an unusual packing of the TTQDs²⁷. Detailed analysis indicates that this superlattice can be explained by one of the previously simulated quasicrystal-approximant models with slight modifications¹¹. As in the previous model, the superlattices are assembled with two basic units: a log unit containing 12 TTQDs and a zip unit containing 20 TTQDs (Fig. 3c, Supplementary Figs. 26, 27, Supplementary Tables 9–12). We find that log- and zip units with intermediary

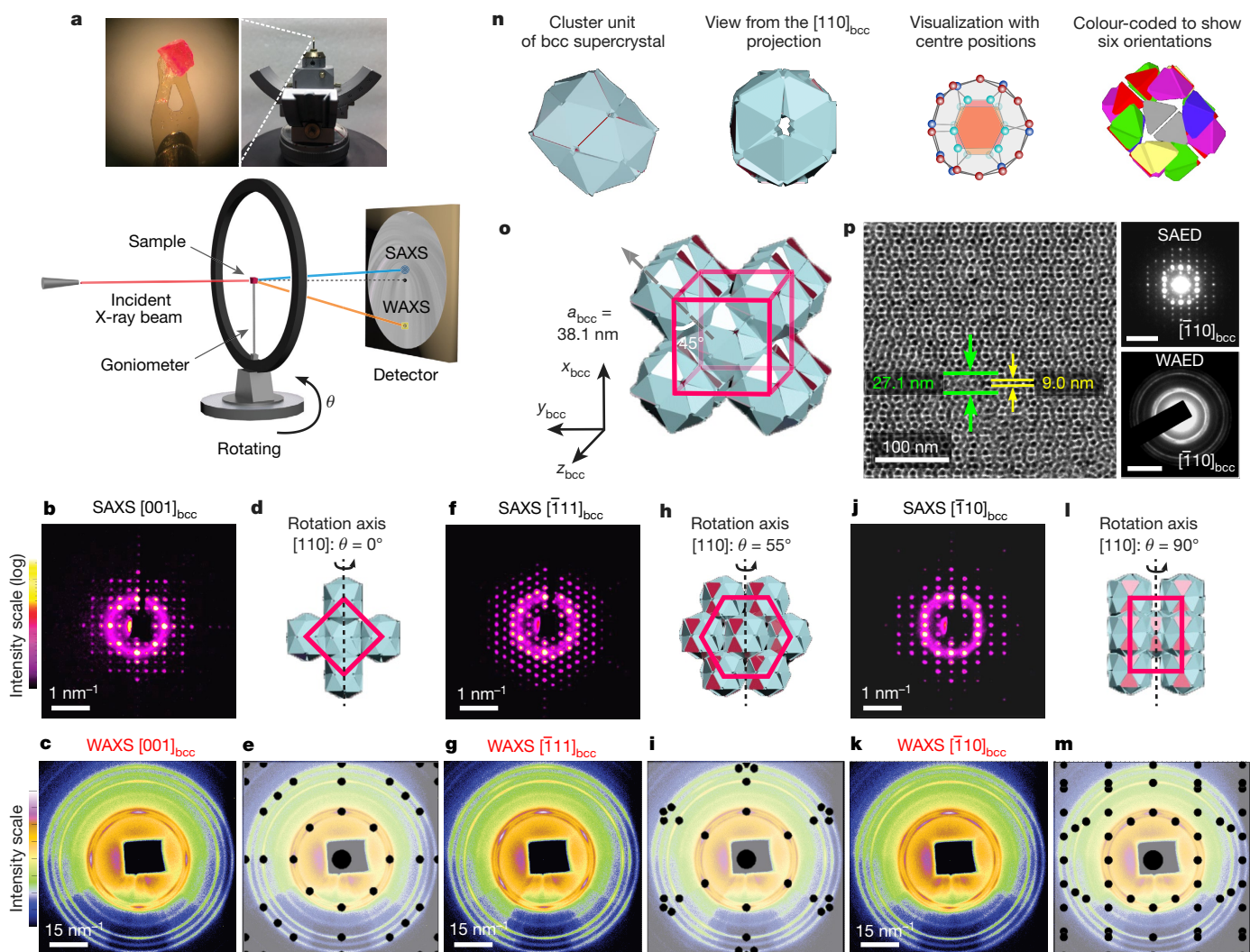


Fig. 2 | Characterization of 3D cluster-based bcc single supercrystals. **a**, Photograph of a piece of bcc supercrystal loaded on a goniometer (top) and a schematic illustration of the synchrotron-based rotational X-ray scattering setup (bottom). **b–m**, 2D images of SAXS (**b, f, j**) and WAXS (**c, g, k**) patterns at three representative crystallographic orientations: $[001]_{\text{bcc}}$ (**b–e**), $[\bar{1}11]_{\text{bcc}}$ (**f–i**) and $[\bar{1}10]_{\text{bcc}}$ (**j–m**). The simulated WAED patterns (**e, i, m**) were generated from computer models (**d, h, l**) at the three crystallographic orientations. **n**, Computer-generated models of

cluster unit from the $[001]_{\text{bcc}}$ projection (left) and from the $[110]_{\text{bcc}}$ projection (middle left), a polyhedron ($3^{24} 5^{12} 6^2$) created by connecting TTQD centre points (middle right) and a cluster model with six-crystal orientation domains classified by colour (right). **o**, Computer-generated model of a unit cell of the 3D cluster-based bcc supercrystals. **p**, TEM image of a monolayer of the cluster unit viewed from the $[\bar{1}10]_{\text{bcc}}$ projection (left) and the corresponding SAED (top right; scale bar, 0.1 nm^{-1}) and WAED (bottom right; scale bar, 2 nm^{-1}) patterns.

tetrahedra can pack well via square–triangle–rhombus tiling (Fig. 3d, Supplementary Figs. 28, 29, Supplementary Tables 10–12). We note that there is no indication of the existence of pentagonal dipyramid units, as seen in the previous model¹¹. The FFT pattern of the proposed model is consistent with the FFT pattern of the TEM images and the corresponding SAED pattern (Supplementary Fig. 28). To validate our model, we conducted structural analysis of all the constituent TTQD orientations inside the log- and the zip units. WAED simulations show that the two groups of zip units inside the superlattices contribute to the simulated electron diffraction patterns with the characteristic quasi-four-fold atomic orientation symmetry and well reproduce the WAED pattern (Fig. 3e, Supplementary Fig. 29, Supplementary Tables 11, 12). No major signals from either the log unit or the intermediary tetrahedra are generated in the simulated diffraction pattern (Supplementary Fig. 29, Supplementary Table 10). In addition, we observe that the superlattice areas are exclusively assembled from either the zip- or the log units (Fig. 3f–i, Supplementary Figs. 30–34, Supplementary Tables 13–16). Figure 3f shows a TEM image with lattice fringes of 9.0 nm and a cross-fringe angle of 58.2° . This ‘zig-zag’ type of superlattice can be replicated by stacking only the zip units. Both the superlattice periodicities and the atomic electron diffraction simulation from a

zip-unit-only packing model can closely duplicate the corresponding reduced two-fold symmetries of the localized SAED and WAED patterns (Fig. 3f, g, Supplementary Fig. 30, Supplementary Table 13). Similarly, a TTQD superlattice resulting exclusively from the log units with lamellar lattice fringes (lamellar length of 9.0 nm) is also observed (Fig. 3h, i). The WAED pattern is consistent with the electron diffraction simulation without showing strongly localized $(10\bar{1}0)_{\text{WZ}}$, $(0002)_{\text{WZ}}$ and $(10\bar{1}1)_{\text{WZ}}$ signals (Fig. 3i, Supplementary Fig. 31, Supplementary Table 14). Taken together, these results demonstrate that the observed 2D superlattices that self-assemble from TTQDs may exhibit a quasicrystal-approximant packing as predicted from the thermodynamic simulation¹¹. We note that this proposed TTQD quasicrystal-approximant packing model cannot be confirmed by the current dataset owing to the high complexity of the 2D superlattices.

We note that the three superstructures assembled from TTQDs have one common structural feature: the preferred facet-to-facet alignment ($\{0002\}_{\text{WZ}}$ -to- $\{0002\}_{\text{WZ}}$ and $\{10\bar{1}1\}_{\text{WZ}}$ -to- $\{10\bar{1}1\}_{\text{WZ}}$). Additional proof of this facet-contacting preference was provided by Fourier-transform infrared spectroscopy (FTIR) (Extended Data Fig. 9, Extended Data Table 1). Compared to the amorphous TTQD powder sample, both the blue shift (about 51 cm^{-1}) of the PO_3 asymmetric stretch and the

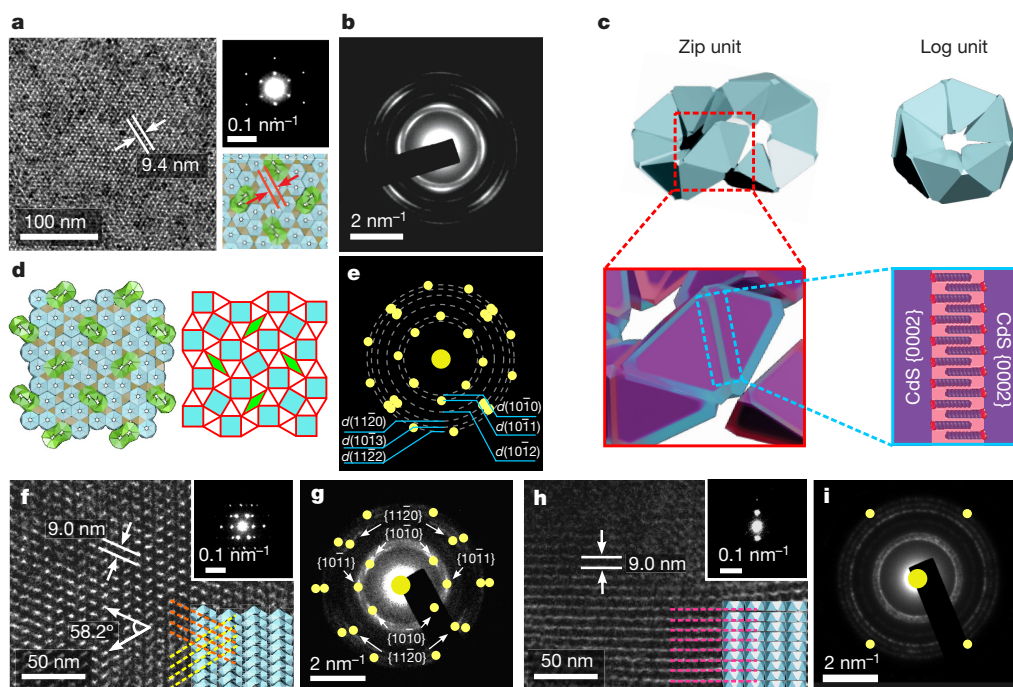


Fig. 3 | Characterization of the 2D superlattice with a tentative quasicrystal-approximant superstructure. **a**, TEM image of a 2D superlattice viewed from the top (left), the corresponding SAED pattern (top right) and a computer-generated illustration of the 2D superlattice (bottom right). **b**, Corresponding WAED pattern for the superlattice area shown in **a**. **c**, Computer-generated models of a zip unit (left) and a log unit (right). **d**, Computer-generated illustration of the 2D superlattice (left) and the tiling (right). **e**, Simulated electron diffraction pattern of the 2D superlattice model displayed in **d**. **f**, TEM image of the side view

of the assembly formed from only zip units, and the corresponding SAED pattern (inset). **g**, WAED pattern and a simulated electron diffraction pattern (yellow dots) from a zip-unit-only model. **h**, TEM image of the side view of the assembly formed from only log units, and the corresponding SAED pattern (inset). **i**, WAED pattern and a simulated electron diffraction pattern (yellow dots) from a log-unit-only model. We note that the slight deviation between the simulated electron diffraction signals and the WAED pattern probably results from small deviations in particle orientations and structural packing defects.

considerably weakened P=O vibration of the ODPAs from the bcc supercrystal indicate the confined state of the ODPAs between the two {0002}_{WZ} facets in one TTQD pair²⁸. This confined state decreases the conformational entropy of the ligand owing to strengthened ligand–ligand interactions, thereby maximizing the structural stability at high complexities^{13,21}. It has been proven that interfacial interaction can be induced solely by directional entropic forces between hard shapes through entropic patchiness upon crowding^{6,14,15}. However, in our case, the increased anisotropic van der Waals interactions between ODPAs ligands, which result in a tendency to form an ordered intermolecular structure between linear hydrocarbon chains^{29,30}, combined with the intrinsic crystal dipole along the [0002]_{WZ} direction, provide additional enthalpic patchiness on the {0002}_{WZ} facet of the TTQDs, resulting in facet alignments with specific selectivity²². As a control, when the supercrystals are formed in a more polar environment, faster supercrystal nucleation and shorter growth periods (hours rather than weeks) are observed. Consequently, instead of the cluster-based bcc supercrystal, a face-centred-cubic-like structure is generated from individual TTQDs, in which neither cluster formation nor orientation alignment of TTQDs are observed owing to the rotational freedom of the TTQDs (Supplementary Figs. 35, 36, Supplementary Table 17). This further demonstrates the role of enthalpy during the facet-to-facet contact process. In addition, facet-to-facet contact decreases the rotational freedom of the TTQDs^{13,23}, thus enabling strong atomic-orientation alignment as seen in the WAED and WAXS measurements, which ultimately enabled the otherwise impossible structural elucidation of these highly complex assemblies.

In conclusion, we found that TTQDs can self-assemble into three distinct superstructures: 1D chiral tetrahelices, 2D quasicrystal-approximant superlattices and 3D cluster-based bcc supercrystals. To our knowledge, these results provide the first experimental observation of complex superstructures assembled from single-component tetrahedral building blocks. By taking advantage of the atomic crystal phase

of the TTQDs and the unique, assembled superstructures, the details of the packing of TTQDs were elucidated using characterization techniques in both real and reciprocal spaces. In addition, we determined that entropy and enthalpy co-induced specific facet contacts, which were the major driving force for the formation of the superstructures in different dimensions. This study not only demonstrates fundamental packing strategies for tetrahedron-shaped nano-objects, but also drives momentum towards the next level of complexity in the expansion of nanocrystal assemblies across atomic, nano and macroscopic materials.

Online content

Any methods, additional references, Nature Research reporting summaries, source data, statements of data availability and associated accession codes are available at <https://doi.org/10.1038/s41586-018-0512-5>.

Received: 18 October 2017; Accepted: 7 August 2018;
Published online 19 September 2018.

- Boles, M. A., Engel, M. & Talapin, D. V. Self-assembly of colloidal nanocrystals: from intricate structures to functional materials. *Chem. Rev.* **116**, 11220–11289 (2016).
- Feng, W. et al. Assembly of mesoscale helices with near-unity enantiomeric excess and light-matter interactions for chiral semiconductors. *Sci. Adv.* **3**, e1601159 (2017).
- Dong, A. G. et al. Binary nanocrystal superlattice membranes self-assembled at the liquid–air interface. *Nature* **466**, 474–477 (2010).
- Lin, H. X. et al. Clathrate colloidal crystals. *Science* **355**, 931–935 (2017).
- Wu, L. H. et al. High-temperature crystallization of nanocrystals into three-dimensional superlattices. *Nature* **548**, 197–201 (2017).
- Boneschanscher, M. P. et al. Long-range orientation and atomic attachment of nanocrystals in 2D honeycomb superlattices. *Science* **344**, 1377–1380 (2014).
- Liu, W. Y. et al. Diamond family of nanoparticle superlattices. *Science* **351**, 582–586 (2016).
- Weidman, M. C., Smilgies, D. M. & Tisdale, W. A. Kinetics of the self-assembly of nanocrystal superlattices measured by real-time in situ X-ray scattering. *Nat. Mater.* **15**, 775–781 (2016).
- Wang, T. et al. Self-assembled colloidal superparticles from nanorods. *Science* **338**, 358–363 (2012).

10. Cabane, B. et al. Hiding in plain view: Colloidal self-assembly from polydisperse populations. *Phys. Rev. Lett.* **116**, 208001 (2016).
11. Haji-Akbari, A. et al. Disordered, quasicrystalline and crystalline phases of densely packed tetrahedra. *Nature* **462**, 773–777 (2009).
12. Gong, J. X. et al. Shape-dependent ordering of gold nanocrystals into large-scale superlattices. *Nat. Commun.* **8**, 14038 (2017).
13. Li, R. et al. Competing interactions between various entropic forces toward assembly of Pt₃Ni octahedra into a body-centered cubic superlattice. *Nano Lett.* **16**, 2792–2799 (2016).
14. Manoharan, V. N. Colloidal matter: Packing, geometry, and entropy. *Science* **349**, 1253751 (2015).
15. Petukhov, A., Tuinier, R. & Vroege, G. Entropic patchiness: Effects of colloid shape and depletion. *Curr. Opin. Colloid Interface Sci.* **30**, 54–61 (2017).
16. Kallus, Y. & Elser, V. Dense-packing crystal structures of physical tetrahedra. *Phys. Rev. E* **83**, 036703 (2011).
17. Torquato, S. & Jiao, Y. Dense packings of the Platonic and Archimedean solids. *Nature* **460**, 876–879 (2009).
18. Conway, J. H. & Torquato, S. Packing, tiling, and covering with tetrahedra. *Proc. Natl Acad. Sci. USA* **103**, 10612–10617 (2006).
19. Chen, E. R., Engel, M. & Glotzer, S. C. Dense crystalline dimer packings of regular tetrahedra. *Discrete Comput. Geom.* **44**, 253–280 (2010).
20. Yang, M. et al. Self-assembly of nanoparticles into biomimetic capsid-like nanoshells. *Nat. Chem.* **9**, 287–294 (2017).
21. Huang, M. J. et al. Selective assemblies of giant tetrahedra via precisely controlled positional interactions. *Science* **348**, 424–428 (2015).
22. Tang, Z., Kotov, N. A. & Giersig, M. Spontaneous organization of single CdTe nanoparticles into luminescent nanowires. *Science* **297**, 237–240 (2002).
23. Boles, M. A. & Talapin, D. V. Self-assembly of tetrahedral CdSe nanocrystals: effective “patchiness” via anisotropic steric interaction. *J. Am. Chem. Soc.* **136**, 5868–5871 (2014).
24. Ghosh, S. et al. Pyramid-shaped wurtzite CdSe nanocrystals with inverted polarity. *ACS Nano* **9**, 8537–8546 (2015).
25. Tan, R. et al. Monodisperse hexagonal pyramidal and bipyramidal wurtzite CdSe–CdS core–shell nanocrystals. *Chem. Mater.* **29**, 4097–4108 (2017).
26. Förster, S. et al. Order causes secondary Bragg peaks in soft materials. *Nat. Mater.* **6**, 888–893 (2007).
27. Hahn, T. *International tables for crystallography* 5th edn, Vol. A, 1–905 (Springer, Dordrecht, 2005).
28. Wan, Y. et al. Enhanced tribology durability of a self-assembled monolayer of alkylphosphonic acid on a textured copper substrate. *Appl. Surf. Sci.* **259**, 147–152 (2012).
29. Grzelczak, M., Vermant, J., Furst, E. M. & Liz-Marzan, L. M. Directed self-assembly of nanoparticles. *ACS Nano* **4**, 3591–3605 (2010).
30. Vaia, R. A., Teukolsky, R. K. & Giannelis, E. P. Interlayer structure and molecular environment of alkylammonium layered silicates. *Chem. Mater.* **6**, 1017–1022 (1994).

Acknowledgements O.C. acknowledges support from the Brown University Startup Fund, the Salomon Award Fund, the IMNI Seed Fund and the UAC grant from the Xerox foundation. The Cornell High Energy Synchrotron Source was supported by the NSF award DMR-1332208. This work was performed, in part, at the Center for Nanoscale Materials, a US Department of Energy Office of Science User Facility, and supported by the US Department of Energy, Office of Science, under contract number DE-AC02-06CH11357. The TEM and SEM measurements were performed at the Electron Microscopy Facility in the Institute for Molecular and Nanoscale Innovation (IMNI) at Brown University.

Reviewer information *Nature* thanks J. Fang, A. Petukhov and the other anonymous reviewer(s) for their contribution to the peer review of this work.

Author contributions Y.N., R.L., R.T., Z.W. and O.C. conceived and designed the experiments. R.T. performed nanocrystal synthesis. Y.N. and R.T. conducted TTQD superstructure formations. R.L. and Z.W. carried out the rotational SAXS and WAXS measurements. Y.N., D.E., Y.A.W. and Y.L. performed the electron microscopy measurements. Y.N., H.Z. and R.L. conducted the data analysis and simulation. O.C. supervised the entire project. Y.N. and O.C. wrote the manuscript. All authors discussed the results and commented on the manuscript.

Competing interests The authors declare no competing interests.

Additional information

Extended data is available for this paper at <https://doi.org/10.1038/s41586-018-0512-5>.

Supplementary information is available for this paper at <https://doi.org/10.1038/s41586-018-0512-5>.

Reprints and permissions information is available at <http://www.nature.com/reprints>.

Correspondence and requests for materials should be addressed to O.C.
Publisher's note: Springer Nature remains neutral with regard to jurisdictional claims in published maps and institutional affiliations.

METHODS

Synthesis of CdSe core quantum dots. The synthesis of CdSe core quantum dots followed a previously reported hot-injection method³¹. 120 mg CdO (99.998%), 560 mg ODP (99%) and 6 g trioctylphosphine oxide (TOPO, 99%) were loaded into a 100 ml flask. The mixture was degassed and heated to 150 °C for 1 h under vacuum. The reaction solution was then heated to 360 °C under nitrogen to form a clear, colourless solution. After adding 4.0 ml trioctylphosphine (TOP, 97%), the temperature was brought up to 380 °C and a freshly prepared Se/TOP (120 mg Se in 1.0 ml TOP) solution was swiftly injected into the flask. When the CdSe core reached the desired size, the reaction was quenched by removing the heating mantle and blowing the outside of the flask with cool air. The CdSe core size was estimated to be 2.7 nm from the first absorption peak. The resulting CdSe core quantum dots were stored in hexane for use in the next step.

Synthesis of CdSe–CdS core–shell quantum dots with a truncated tetrahedral shape. The quantum dots with edge-truncated tetrahedral shapes were synthesized using a CdS-shell growth protocol we developed recently with minor modifications^{25,32}. In a typical reaction, 100 nmol of CdSe cores were purified once by washing with acetone. The nanocrystals were loaded into a 100 ml three-neck flask with a solvent mixture of 2 ml 1-octadecene (ODE, 90%) and 2 ml oleylamine (OAm, 70%). The reaction mixture was degassed under vacuum at room temperature for 1 h and 120 °C for 10 min to remove hexane, water and oxygen. The reaction mixture was then heated to 310 °C under nitrogen for shell growth. When the temperature reached 240 °C, solutions of Cd-oleate (4-monolayer equivalent of CdS shell) and 1-octanethiol (1.2 equivalent of Cd-oleate), each dissolved in 2 ml of ODE were simultaneously added dropwise using a syringe pump at an injection rate of 2 ml h⁻¹. One hour after the injection was complete, the reaction was stopped by removing the heating mantle and cooling to room temperature by blowing the outside of the flask with cool air. The product was purified by three rounds of precipitation and redispersion using acetone/methanol and hexane. The particles were finally suspended in around 2 ml of hexane for the fabrication of superlattices.

Formation of nanocrystal superstructures from TTQDs. The nanocrystal superstructures were created through solvent (hexane) evaporation. Various nanocrystal superstructures were made by tuning the evaporation speed and the concentration of the nanocrystals.

1D tetrahedral assemblies were created from a 0.2 mg ml⁻¹ solution of TTQD in hexane. One drop (around 20 µl) of the solution was dropped on a TEM grid placed on a piece of silicon wafer. The evaporation was complete within few seconds.

2D superlattice assemblies were created from a 2.0 mg ml⁻¹ solution of TTQD in toluene. One drop (around 20 µl) of the solution was dropped on a TEM grid placed on a piece of silicon wafer and the evaporation was complete in around 30 s.

3D bcc-supercrystal assemblies were created from a 20 mg ml⁻¹ solution of TTQD in hexane through slow evaporation. We placed 5 ml of solution in a 20-ml capped glass vial. The evaporation was complete in two weeks.

Monolayer superlattices of a bcc supercrystal were created from a 20 mg ml⁻¹ solution of TTQD in hexane through slow evaporation. We placed a TEM grid on the bottom of a 5-ml glass vial, 0.1 ml of solution was added and the vial was capped. The evaporation was complete in around 24 h.

Interface assemblies of TTQDs were created through a slow destabilization method³³. 2 ml of a TTQD solution in hexane was placed in a 5 ml glass vial and 2 ml of ethanol was slowly added. The layers of the polar phase (ethanol) and the nonpolar phase (TTQD/hexane solution) were initially clearly separated, but slowly merged together to form one liquid phase through interfacial diffusion (several hours). A silicon chip can also be placed inside the vials as a substrate for growing the supercrystal.

Characterization techniques. Ultraviolet–visible absorption spectra were measured using an Agilent Technologies Cary 5000 UV-Vis-NIR Spectrophotometer. Typically, the samples were dissolved in hexane for the measurements.

Photoluminescence measurements were performed using an Edinburgh Instruments Fluorescence Spectrometer FS5. Typically, the samples were dissolved in hexane for these measurements.

TEM measurements were performed on a JEOL-2100F operated at 200 kV and a FEI-Philips CM20 operated at 200 kV. For the solution samples, such as the TTQD building blocks, one drop of the hexane solution with fine concentration adjustment was dropped onto a 300-mesh copper TEM grid placed on filter paper and dried under ambient conditions. 1D tetrahedral, 2D superlattice and 3D bcc-supercrystal assemblies were formed on TEM grids placed on a silicon wafer or in a glass vial. For the 3D bcc-supercrystal sample, we carefully selected a small

piece of the sample, gently placed it on a TEM grid and sliced it into thinner pieces. We note that the bcc-supercrystal samples were fragile and extra care was needed.

WAED and SAED measurements were carried out on a JEOL-2100F operated at 200 kV. Camera lengths of 20 cm and 200 cm were typically used for WAED and SAED, respectively.

HAADF scanning TEM (STEM) and STEM–energy dispersive X-ray spectroscopy (EDS) mapping was performed on a FEI Talos F200X TEM/STEM running at 200 kV equipped with a SuperX EDS detector. SEM measurements were performed on a LEO 1530 operated at 3 kV.

FTIR measurements were performed on a Jasco FT/IR 4100. The solution sample was directly dropped, or the solid sample was placed onto a NaCl pellet.

Synchrotron-based SAXS and WAXS measurements were performed at the B1 station of the Cornell High Energy Synchrotron Source (CHESS), Cornell University. Using a double circular pinhole aligned tube, monochromatic X-rays at a collimated energy of 25.514 keV were reduced to a small beam with a diameter of 100 microns. SAXS and WAXS images were collected simultaneously using a large area Mar345 detector. A mixture of CeO₂ powders was used to calibrate the sample-to-detector distances and associated detector seating parameters.

A single bcc supercrystal was loaded onto a MiTeGen mesh grid, which was subsequently mounted on the home-made two-circle rotating diffractometer. The bcc supercrystal was aligned parallel to a desirable rotation axis. Upon X-ray illumination, a series of SAXS and WAXS images were collected during sample rotation. An angular rotation step of 1° was used, and the full dataset was collected by rotation of θ over an angular range of 180°.

Analysis software. For analysis, a Fit2D program (www.esrf.eu/computing/scientific/FIT2D) was used to integrate the collected SAXS and WAXS images into 1D patterns. A Multi-Peak Fitting 2.0 package in Igor Pro version 6.37 (WaveMetrics) was used for the XRD peak analyses. CrystalMaker version 9.2 (CrystalMaker Software Ltd) was used for simulation of X-ray and electron diffraction results. Computer model construction was carried out using Autodesk 3dsMax (Autodesk). ImageJ (<https://imagej.nih.gov/ij/>) was used for 2D-FFT analysis. The WAED and WAXS patterns of the 2D superlattice and 3D bcc supercrystal were simulated using the ‘Single-electron diffraction’ function in CrystalMaker. Typically, the observed WAED and WAXS patterns resulted from multiple crystal domains. Diffraction patterns for each domain were simulated using the ‘Single-electron diffraction’ function in CrystalMaker and the resulting patterns were combined using Adobe Photoshop based on determined crystal orientations and viewing directions.

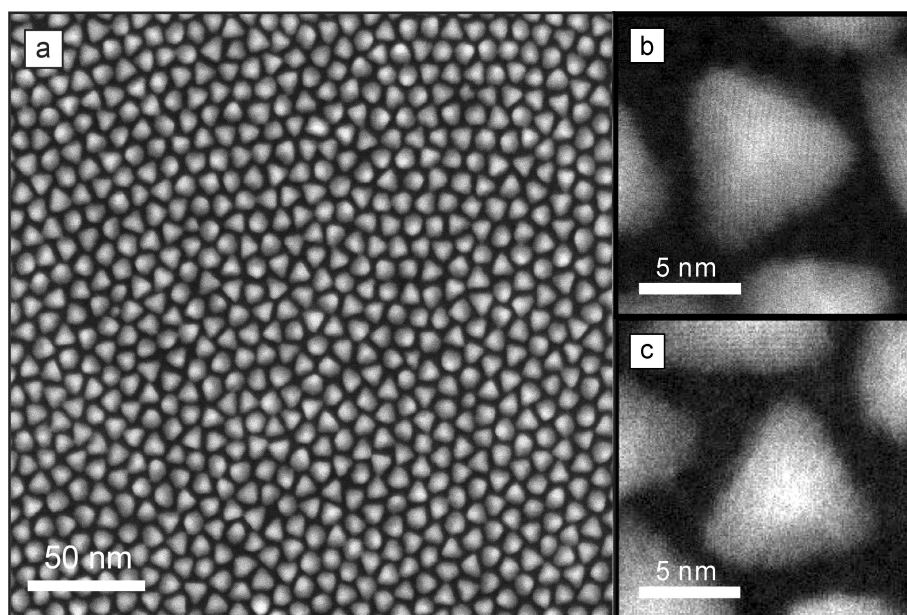
SAXS patterns of the bcc supercrystal were simulated using two methods (see Supplementary Information for details): method (i), 2D-FFT from computer-generated models of the superstructure; and method (ii), 3D-mesh pixel-based calculation of the multiplication of the form factor and the structure (lattice) factor. In method (i), a computer model of the bcc-supercrystal structure was first constructed using Autodesk 3dsMax. Smaller building blocks were used for obtaining 2D-FFT images. The computer model of the bcc-supercrystal structure was rendered from multiple projections corresponding to the observed SAXS patterns such as the [100]_{bcc}, the $\bar{1}11$ _{bcc} and the $\bar{1}10$ _{bcc} projections. 2D-FFT using ImageJ was applied to these superlattice model images. The obtained FFT patterns were further processed for ease of visualization using the ‘Gaussian Blur’ function in Adobe Photoshop, in which the FFT spots were broadened while maintaining the intensity profiles of each signal. For method (ii), we used a 2D meshgrid method and calculated an intensity for each pixel for the simulation of the 2D SAXS pattern. The details were described in the Supplementary Information section entitled ‘SAXS simulation Method (ii): Multiplication of the form factor and the structure (lattice) factor’.

Sample size. No statistical methods were used to predetermine sample size.

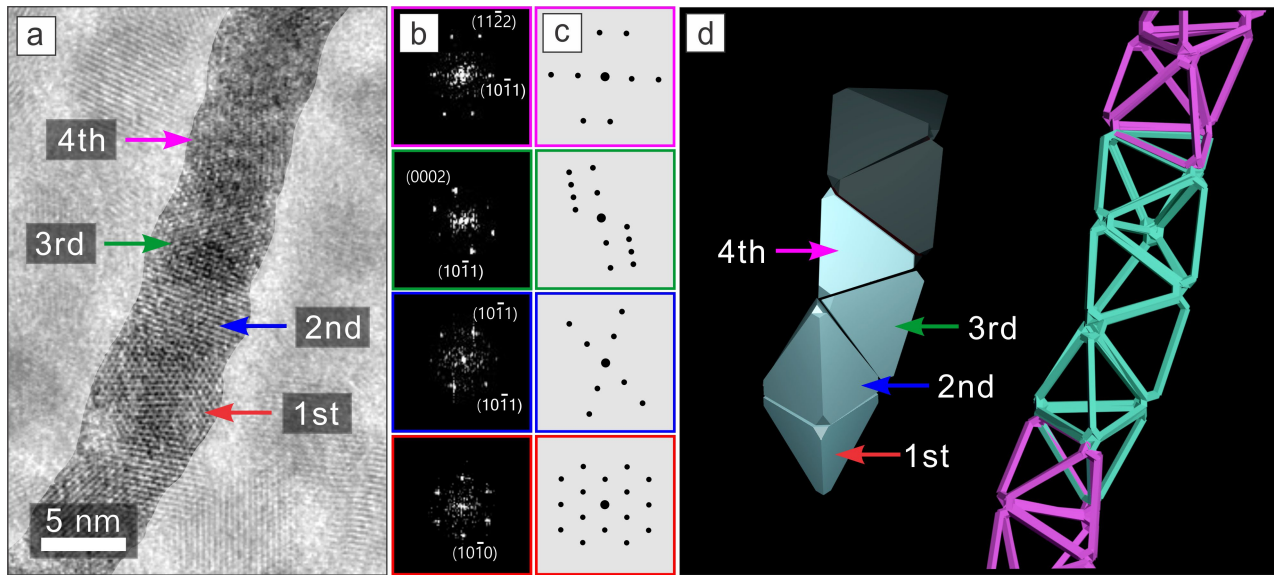
Data availability

The data supporting the findings of this study are available from the corresponding author upon reasonable request.

- Carbone, L. et al. Synthesis and micrometer-scale assembly of colloidal CdSe/CdS nanorods prepared by a seeded growth approach. *Nano Lett.* **7**, 2942–2950 (2007).
- Chen, O. et al. Compact high-quality CdSe–CdS core–shell nanocrystals with narrow emission linewidths and suppressed blinking. *Nat. Mater.* **12**, 445–451 (2013).
- Talapin, D. V. et al. CdSe and CdSe/CdS nanorod solids. *J. Am. Chem. Soc.* **126**, 12984–12988 (2004).

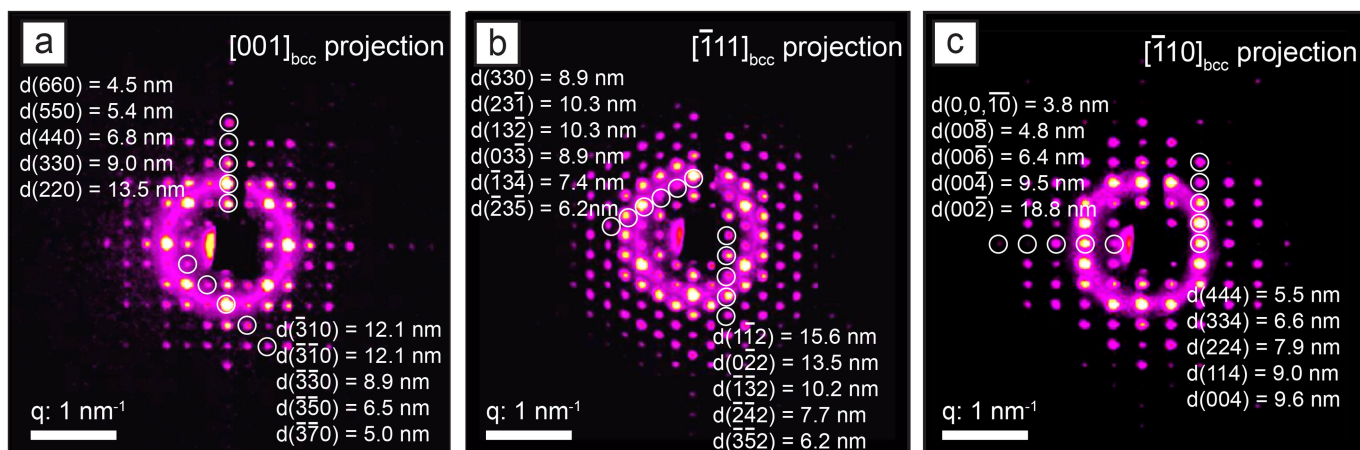


Extended Data Fig. 1 | HAADF-STEM images. a–c, HAADF-STEM images of TTQDs at low (a) and high (b, c) magnification.



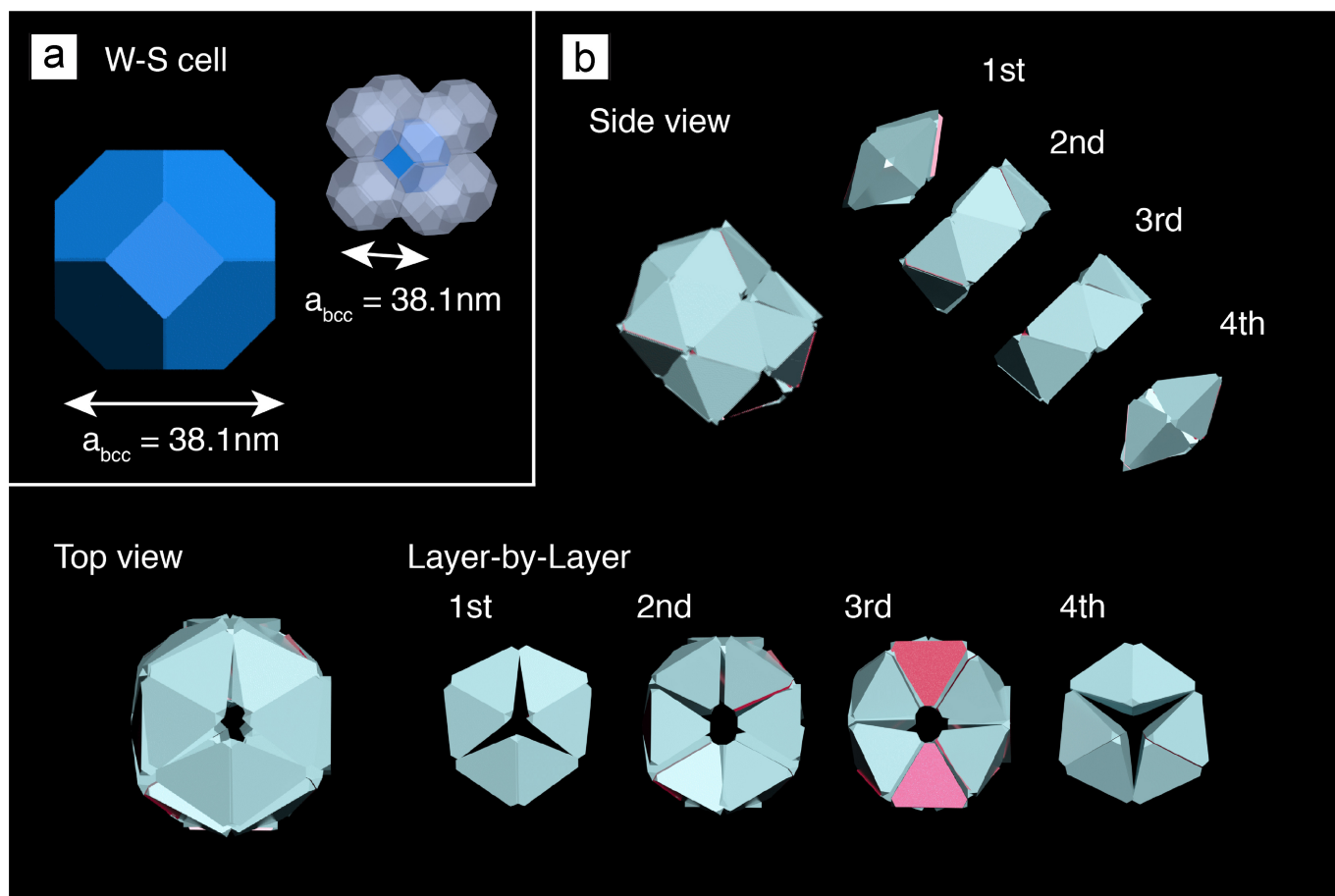
Extended Data Fig. 2 | Tetrahelix with a left-handed (counterclockwise) spiral. a, HR-TEM image of a tetrahelical assembly. **b**, FFT patterns corresponding to the four consecutive domains.

c, The corresponding simulated electron diffraction patterns of the four domains. **d**, The corresponding schematic illustration of the tetrahelix.



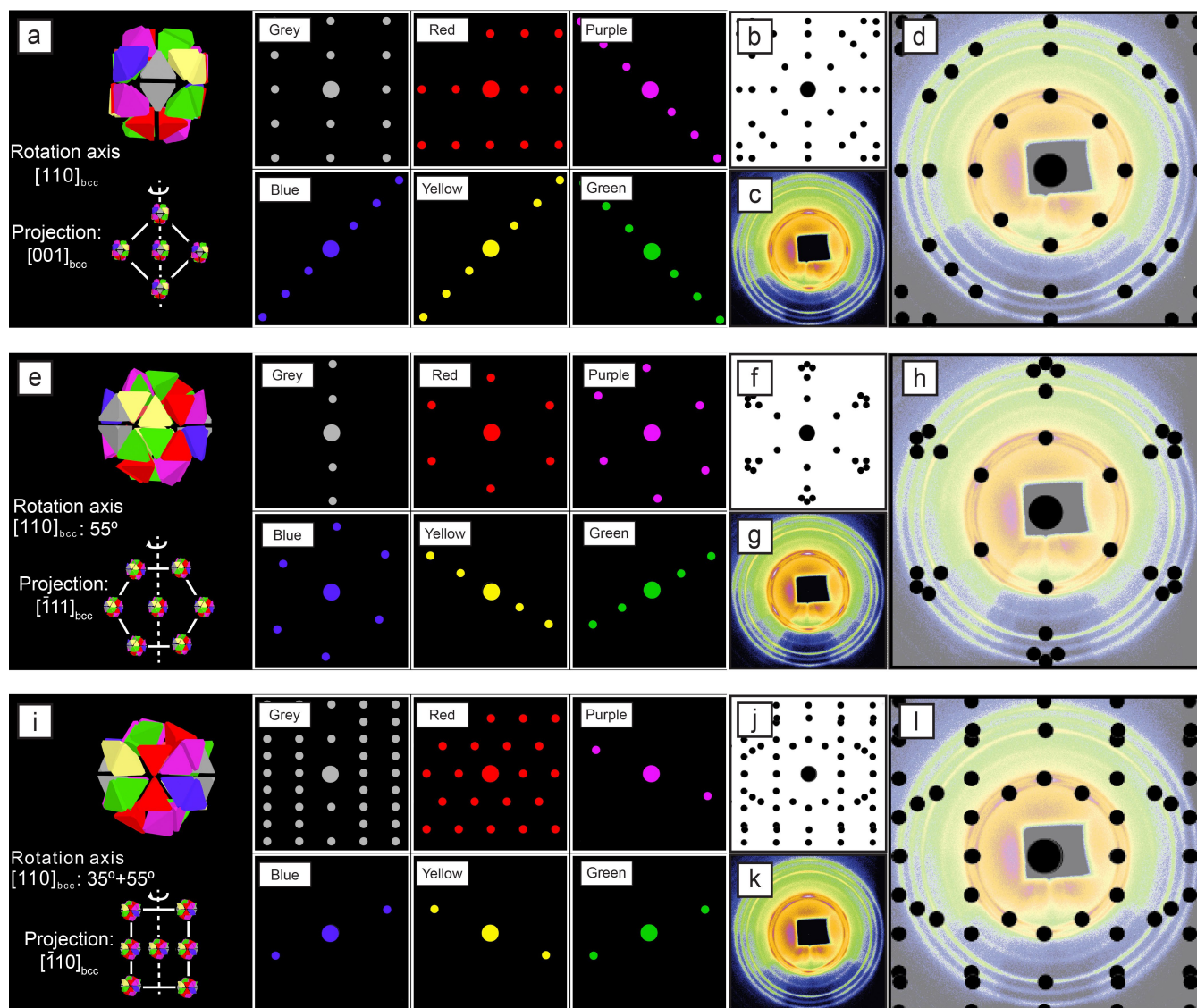
Extended Data Fig. 3 | Representative SAXS patterns from different projections obtained from rotational SAXS measurements along the

$[110]_{\text{bcc}}$ axis. a–c, $[001]_{\text{bcc}}$ projection (a), $[\bar{1}11]_{\text{bcc}}$ projection (b) and $[\bar{1}10]_{\text{bcc}}$ projection (c). The d -spacings of representative spots are labelled.



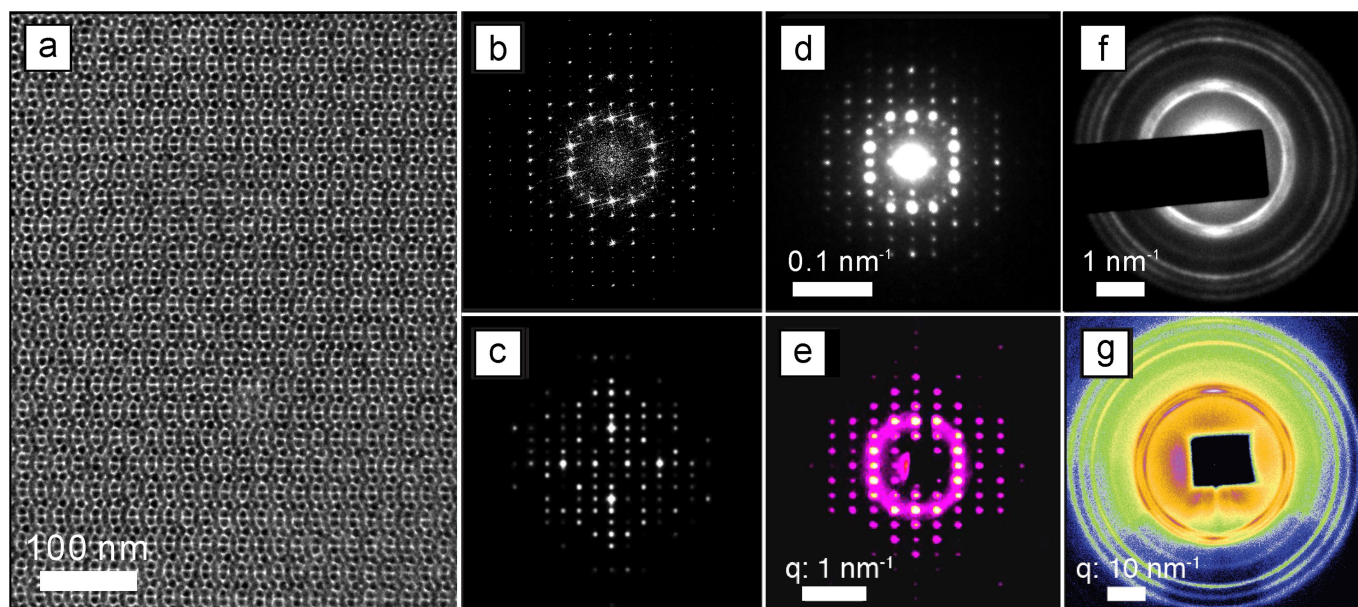
Extended Data Fig. 4 | Construction of a cluster-unit building block of the bcc-supercrystal solid from 36 TTQDs. a, Wigner-Seitz (W-S) cell of a bcc crystal structure. **b,** Schematic illustrations of the assembled and disassembled ‘ball-like’ cluster-units comprising 36 TTQDs, viewed

from the side and the top. We note that ‘bcc’ represents another level of ‘cluster-based bcc superlattice’, and if a less dense and open structure is considered, a slight symmetry-breaking of the cluster does not modify the bcc structure.



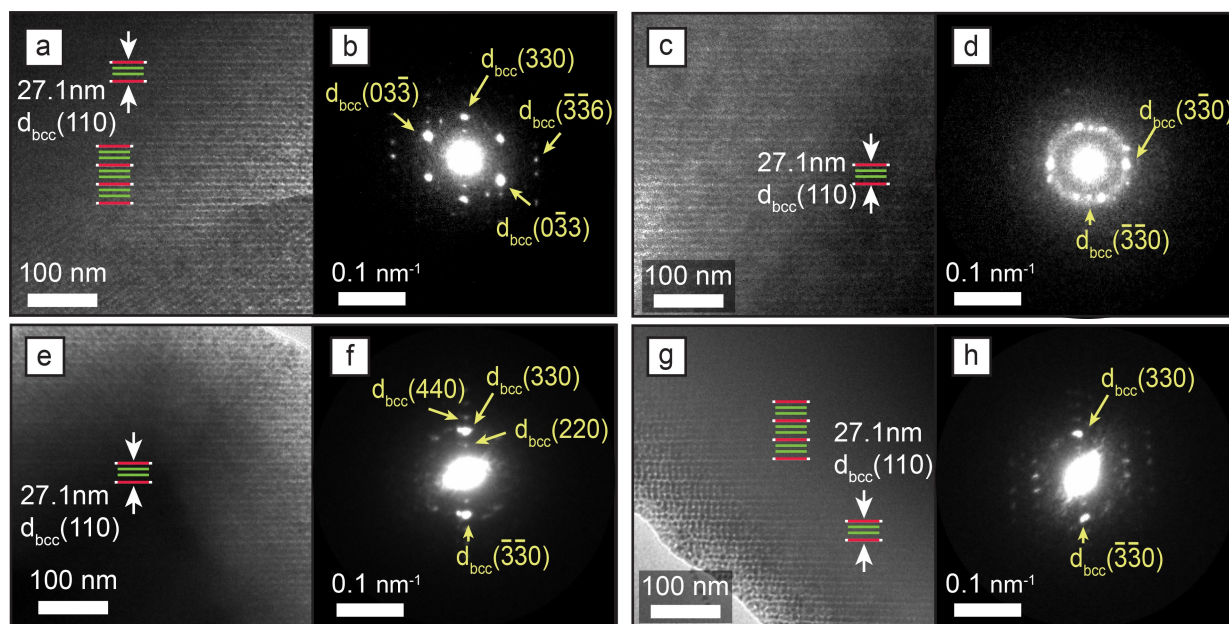
Extended Data Fig. 5 | Simulations of the WAXS patterns obtained from the rotational WAXS measurements along the $[110]_{\text{bcc}}$ axis. **a–l**, Simulations of the WAXS patterns for the $[001]_{\text{bcc}}$ projection (**a–d**), the $[\bar{1}11]_{\text{bcc}}$ projection (**e–h**) and the $[\bar{1}10]_{\text{bcc}}$ projection (**i–l**). In the cluster unit, six atomic orientations were used which are colour-coded in the computer-generated models. The orientations are classified using grey,

red, purple, blue, yellow and green colours in the model (leftmost panels in **a**, **e**, **i**) and in the corresponding simulated patterns for each orientation (right panels in **a**, **e**, **i**). Simulated WAXS patterns were generated by overlapping six orientations (**b**, **f**, **j**). The experimentally observed WAXS patterns (**c**, **g**, **k**) were compared with the resulting simulated patterns (**d**, **h**, **l**).



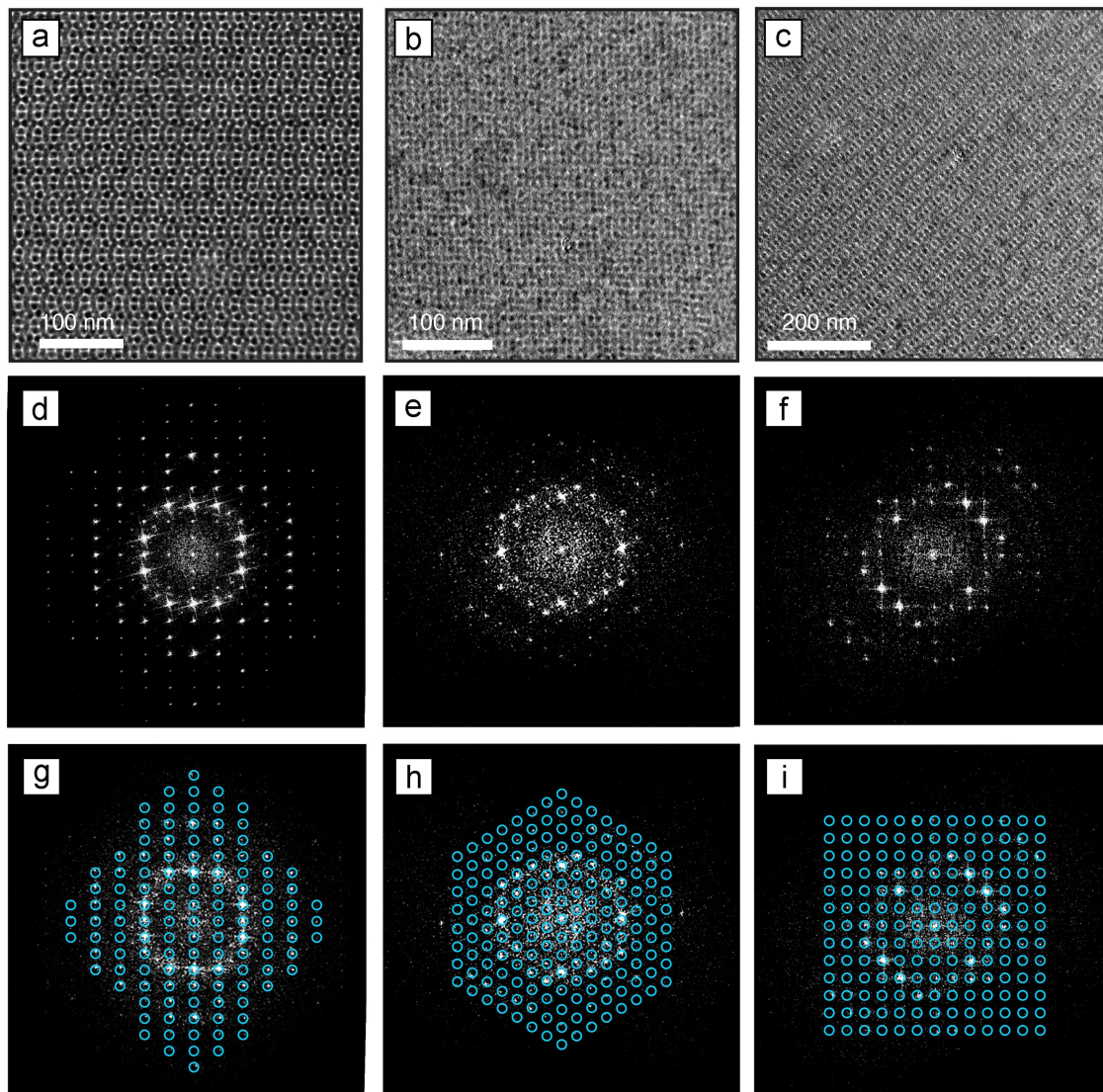
Extended Data Fig. 6 | Comparison between simulations and experimental results using characterization techniques in real and reciprocal spaces. **a**, TEM image for the monolayer superlattice of a bcc supercrystal along the $[\bar{1}10]_{\text{bcc}}$ projection. **b**, The FFT pattern of the image in **a**. **c**, SAXS method (ii) simulation of a bcc supercrystal from the $[\bar{1}10]_{\text{bcc}}$ projection (shown in Supplementary Figs. 19 and 20b). **d**, SAED pattern from the superlattice area of **a**. **e**, SAXS pattern of a bcc supercrystal

from the $[\bar{1}10]_{\text{bcc}}$ projection. **f**, WAED pattern from the superlattice area of **a**. **g**, WAXS pattern from a bcc supercrystal from the $[\bar{1}10]_{\text{bcc}}$ projection. We note that **b–e** all exhibited similar patterns in terms of the signals and the intensity profiles, indicating the validity of our approach to the identification of complex structures by iterating real and reciprocal spaces using the FFT of the model and the TEM images, diffraction patterns such as SAED and SAXS, and TEM images.



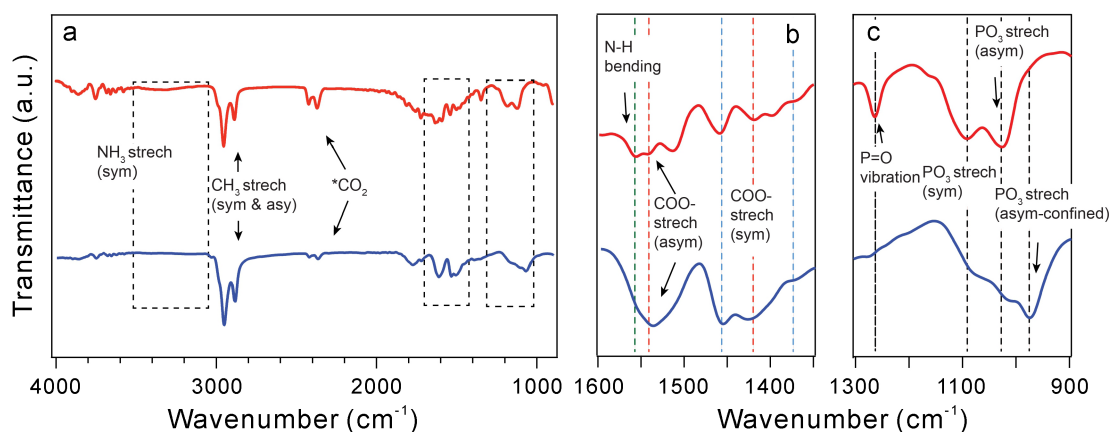
Extended Data Fig. 7 | TEM and SAED of bcc-supercrystal solids with tri-line contrast. a–h, Additional TEM images for bcc-supercrystal solids (a, c, e, g) and the corresponding SAED patterns (b, d, f, h). We note that although the TEM images all showed similar patterns with tri-line contrast (a, c, e, g), the SAED patterns for the selected areas gave different patterns (b, d, f, h). This discrepancy is due to a deeper penetration depth of the electron beam used in the SAED measurement than for the 2D

TEM imaging. This result indicates that these bcc supercrystals have a three-layer structure, and that the out-of-plane direction is parallel to the $[110]_{bcc}$ direction. We also assigned SAED patterns to the corresponding projections: the $[111]_{bcc}$ projection (b) and the $[100]_{bcc}$ projection (d). The SAED patterns shown here were obtained from a bcc supercrystal without fixed rotational orientations; therefore, some of the SAED patterns did not have clear bcc-oriented patterns such as those in f and h.



Extended Data Fig. 8 | TEM tilting experiment with monolayer superlattices of a bcc-supercrystal solid. a–c, TEM images from $[\bar{1}10]_{\text{bcc}}$ (a), $[\bar{1}11]_{\text{bcc}}$ (b) and $[010]_{\text{bcc}}$ (c) projections. **d–i,** The

corresponding FFT patterns from the TEM images shown in a–c. These patterns were assigned to the $[\bar{1}10]_{\text{bcc}}$ (d, g), $[\bar{1}11]_{\text{bcc}}$ (e, h) and $[010]_{\text{bcc}}$ (f, i) projections.



Extended Data Fig. 9 | FTIR spectra of an amorphous powder sample of the TTQDs and the bcc-supercrystal solid. In all panels, the spectra of the amorphous powder are shown in red and the bcc-supercrystal solid in blue. **a**, Full FTIR spectra. **b**, An expansion in the region of $1,600\text{ cm}^{-1}$ to $1,350\text{ cm}^{-1}$, which shows various peaks: a characteristic N–H bend appearing at $1,559\text{ cm}^{-1}$ (green dotted line); asymmetric and symmetric stretching of the carboxylate group ($-\text{COO}^-$) appearing at $1,537\text{ cm}^{-1}$ and $1,430\text{ cm}^{-1}$ respectively (red dotted lines); a C–H scissoring bend at $1,458\text{ cm}^{-1}$ and $\text{CH}_3\text{--C--H}$ bending at $1,378\text{ cm}^{-1}$ (blue dotted lines). The peak separation between asymmetric and symmetric stretching of the carboxylate group ($-\text{COO}^-$) is 107 cm^{-1} , which suggests bidentate binding and chelate formation. **c**, An expansion in the region of $1,300\text{ cm}^{-1}$

to 900 cm^{-1} , the P–O stretching region of the FTIR spectrum of ODPA molecules. The following peaks are observed: P=O vibration; PO_3 symmetric stretches in the range of $1,000\text{ cm}^{-1}$ to $1,150\text{ cm}^{-1}$; PO_3 asymmetric stretches in the range of 950 cm^{-1} to $1,030\text{ cm}^{-1}$. The PO_3 asymmetric stretch of the bcc-supercrystal sample is blue-shifted by 51 cm^{-1} (from $1,029\text{ cm}^{-1}$ to 978 cm^{-1}) when compared with the amorphous TTQD powder sample. The P=O vibration was also considerably weakened in the bcc-supercrystal sample in comparison to the amorphous TTQD powder sample. Similar changes have been observed previously, for example in ref. ²⁸, indicating a higher packing density of ODPA molecules in a confined state as a result of sandwiching between two atomic planes (that is, two $\{0002\}_{\text{WZ}}$ crystal facets).

Extended Data Table 1 | FTIR peak assignments for TTQDs and the bcc-supercrystal solid

peak (cm ⁻¹)	intensity	assignment	ref	amorphous TTQDs (cm ⁻¹)	<i>bcc-supercrystal</i> (cm ⁻¹)
3005	Medium	C-H stretch in C=C-H	25,S7	3001	3001
2924	Strong	CH ₂ asymmetric stretch	25,S7	2919	2919
2854	Strong	CH ₂ symmetric stretch	25,S7	2850	2850
1460-1470	Strong	C-H scissoring bending	S8,9	1458	1458
1378	Medium	CH ₃ -C-H bending	25,S9	1378	1378
1556-1540	Strong	COO- asymmetric stretch	S7,8	1537	1537
1418-1404	Strong	COO- symmetric stretch	S7,8	1430	1430
3000-3300	Weak	N-H stretch	25,30,S10	weak	absent
1558	Weak	N-H bending	25,30,S10	weak	absent
1261	Strong	P=O vibration	28,S11-14	1260	Weak
1000-1150	Strong	PO ₃ symmetric stretch	28,S11-14	1080	1088
950-1030	Strong	PO ₃ asymmetric stretch	28,S11-14	1029	978

The spectra are shown in Extended Data Fig. 9.